

Microstructure and microwave surface resistance of YBCO films deposited under different oxygen pressures

Zhi-Bo Sheng(盛智博), Fu-Cong Chen(陈赋聪), Pei-Yu Xiong(熊沛雨), Qi-Ru Yi(易栖如), Jie Yuan(袁洁), Yu Chen(陈雨), Yue-Liang Gu(顾月良), Kui Jin(金魁), Huan-Hua Wang(王焕华), Xiao-Long Li(李晓龙), and Chen Gao(高琛)

Citation: Chin. Phys. B, 2025, 34 (**4**): 046105. DOI: 10.1088/1674-1056/adb261
Journal homepage: http://cpb.iphy.ac.cn; http://iopscience.iop.org/cpb

What follows is a list of articles you may be interested in

High-burn-up structure evolution in polycrystalline UO_2: Phase-field modeling investigation

Dan Sun(孙丹), Yanbo Jiang(姜彦博), Chuanbao Tang(唐传宝), Yong Xin(辛勇), Zhipeng Sun(孙志鹏), Wenbo Liu(柳文波), and Yuanming Li(李垣明)
Chin. Phys. B, 2025, 34 (**2**): 026102. DOI: 10.1088/1674-1056/ad9c42

Microstructure and magnetic properties of FeCoZr(Mo)BGe nanocrystalline alloys

Wanqiu Yu(于万秋), Yanxiang Sun(孙筵翔), Lihua Liu(刘立华), and Pingli Zhang(张平丽)
Chin. Phys. B, 2025, 34 (**1**): 016102. DOI: 10.1088/1674-1056/ad5a77

Correlation of microstructure and magnetic softness of Si-microalloying FeNiBCuSi nanocrystalline alloy revealed by nanoindentation

Benjun Wang(汪本军), Wenjun Liu(刘文君), Li Liu(刘莉), Yu Wang(王玉), Yu Hang(杭宇), Xinyu Wang(王新宇), Mengen Shi(施蒙恩), Hanchen Feng(冯汉臣), Long Hou(侯龙), Chenchen Yuan(袁晨晨), Zhong Li(李忠), and Weihuo Li(李维火)
Chin. Phys. B, 2024, 33 (**12**): 126101. DOI: 10.1088/1674-1056/ad84c8

Visualizing extended defects at the atomic level in a $Bi_2Sr_2CaCu_2O_{8+\delta}$ superconducting wire

Kejun Hu(胡柯钧), Shuai Wang(王帅), Boyu Li(李泊玉), Ying Liu(刘影), Binghui Ge(葛炳辉), and Dongsheng Song(宋东升)
Chin. Phys. B, 2024, 33 (**9**): 096101. DOI: 10.1088/1674-1056/ad6ccd

Electronic effects on radiation damage in α-iron: A molecular dynamics study

Lin Jiang(江林), Min Li(李敏), Bao-Qin Fu(付宝勤), Jie-Chao Cui(崔节超), and Qing Hou(侯氢)
Chin. Phys. B, 2024, 33 (**3**): 036103. DOI: 10.1088/1674-1056/ad0ec4

Microstructure and microwave surface resistance of YBCO films deposited under different oxygen pressures

Zhi-Bo Sheng(盛智博)[1], Fu-Cong Chen(陈赋聪)[2], Pei-Yu Xiong(熊沛雨)[2], Qi-Ru Yi(易栖如)[1], Jie Yuan(袁洁)[1,2], Yu Chen(陈雨)[3], Yue-Liang Gu(顾月良)[4], Kui Jin(金魁)[1,2], Huan-Hua Wang(王焕华)[3], Xiao-Long Li(李晓龙)[4], and Chen Gao(高琛)[1,†]

[1] *School of Physical Sciences, University of Chinese Academy of Sciences, Beijing* 100049, *China*
[2] *Institute of Physics, Chinese Academy of Sciences, Beijing* 100190, *China*
[3] *Institute of High Energy Physics, Chinese Academy of Sciences, Beijing* 100049, *China*
[4] *Shanghai Advanced Research Institute, Chinese Academy of Sciences, Shanghai* 200120, *China*

(Received 5 November 2024; revised manuscript received 23 January 2025; accepted manuscript online 5 February 2025)

$YBa_2Cu_3O_{7-x}$ (YBCO) films with low microwave surface resistance (R_S) are essential for high temperature superconducting microwave devices. The oxygen pressure during deposition has been found to influence R_S significantly. In this work, we deposited highly *c*-axis aligned YBCO films on single crystal MgO (001) substrates under different oxygen pressures via pulsed laser ablation. Their detailed microstructure was characterized with three-dimensional reciprocal space mapping (3D-RSM) method and their microwave surface resistance was also measured with resonant cavity perturbation method. We found that the variation of oxygen pressure can affect film microstructure, including grain orientation distribution and the concentration of crystal defects. The microstructure modulation can explain R_S dependence on the oxygen pressure.

Keywords: microstructure, microwave surface resistance, reciprocal space mapping, YBCO films

PACS: 61.05.cp, 74.72.–h, 91.60.Ed, 68.55.–a

DOI: 10.1088/1674-1056/adb261 **CSTR:** 32038.14.CPB.adb261

1. Introduction

Microwave device is a major application of high temperature superconductor (HTSC) due to its low surface resistance (R_S). For example, microstrip filters fabricated with HTSC films can show excellent performance such as high quality factor, negligible insertion loss and deep out-of-band rejection, which can improve the sensitivity and selectivity of microwave systems.[1] Furthermore, HTSC with critical temperature above 77 K opens the door of cooling superconducting devices by liquid nitrogen with a relatively simple mechanical refrigerators, enabling the wide range industrial application of superconductivity.[2]

One class of the HTSC is the superconducting cuprates. These cuprates present an oxygen deficient perovskite structure which contains edge-sharing CuO_2 planes separated by layers composed of rare-earth metals and oxygen.[3] The overlap between the Cu 3d and O 2d atomic orbitals allows hole carries to transfer to CuO_2 planes, which drives the system into superconducting state. Therefore, superconductivity in these cuprates shows high anisotropy.[4] Among them, $YBa_2Cu_3O_{7-x}$ (YBCO) is the first synthesized cuprate HTSC with T_c above liquid nitrogen temperature. This material is also special for exhibiting a large upper critical field and an extremely short superconducting coherence length (about 1.3 nm in CuO_2 planes and 0.2 nm normal to CuO_2 planes at the critical temperature[5]), due to very high binding energy inside the Cooper pairs.[6]

YBCO has been the key material for many applications because of relatively high critical temperature and critical current.[7–10] YBCO HTSC thin films have been used to construct narrow bandpass microstrip filters at 10 GHz.[11,12] In order to further improve the performance of YBCO devices, researchers have devoted to improving their electrical properties,[13–19] and found that oxygen pressure during film deposition can influence R_S significantly.[20] It is suggested that microstructure variation with the change of oxygen pressure might cause the R_S difference.[21]

Based on synchrotron radiation (high brightness, high collimation, etc.) and two-dimensional (2D) x-ray detectors, the three-dimensional reciprocal space mapping (3D-RSM) experiment can record a large volume of reciprocal space with relatively high resolution in reasonable time.[22,23] As grains with same orientation form one set of diffraction patterns in reciprocal space, 3D-RSM can resolve the grain orientations from the diffraction patterns. Furthermore, 3D-RSM can also provide the information on the average grain size and content from the width and intensity of the corresponding diffraction peaks, respectively. Therefore, adequate microstructure information, such as grain orientation, grain size and grain content, can be addressed by 3D-RSM. With these advantages, the syn-

†Corresponding author. E-mail: gaochen@ucas.edu.cn

© 2025 Chinese Physical Society and IOP Publishing Ltd. All rights, including for text and data mining, AI training, and similar technologies, are reserved.

chrotron based 3D-RSM has become a powerful method on microstructure characterization, e.g., the identification of the coherent twin relationship and the recognition of domains.[24]

In this work, highly *c*-axis aligned YBCO films were deposited on single crystal MgO (001) substrate under different oxygen pressures via pulsed laser deposition (PLD). Their microstructures and microwave surface resistances were characterized with 3D-RSM and resonant cavity perturbation technique, respectively. Then the correlation between microwave surface resistance and microstructure was discussed.

2. Materials and methods

2.1. Film deposition

YBCO films were deposited on single crystal MgO (001) substrates by pulsed laser deposition method. The laser wavelength, pulse energy and pulse repetition were 355 nm, 280 mJ, and 4 Hz, respectively. The deposition duration for each film was 40 min and the substrate temperature were kept at 740 °C during the deposition. The films deposited under 0.25 Torr (1 Torr = 1.33322×10^2 Pa), 0.30 Torr, and 0.60 Torr oxygen pressure are labeled as sample #1, sample #2, and sample #3. After the deposition, growth chamber was filled with 1-atm (1 atm = 1.01325×10^5 Pa) oxygen and the films were annealed at 630 °C for 20 min.

2.2. Microstructure characterization

Microstructure was characterized by 3D-RSM method at 1W1A Diffuse x-ray Scattering Station in Beijing Synchrotron Radiation Facility and BL02U2 Surface Diffraction Station in Shanghai Synchrotron Radiation Facility. Shown in Fig. 1(a) is the schematic diagram of experimental set-up: the diffractometer provides the rotational degrees of freedom of the sample, and an array detector records the diffraction patterns. When an x-ray beam irradiates on the sample at an incident angle ω, those reciprocal lattice points happened falling on the Ewald sphere fulfill the Laue law and will be diffracted to the 2θ angle (Fig. 1(b)). Meanwhile, the array detector spans a diffraction angle on both δ and υ circle in the real space, which represents a curved slice in the reciprocal space (Fig. 1(b)), i.e., the diffraction intensity in this angle range can be recorded simultaneously by the array detector. In experiment, by coordinating rotation of the sample, a series of curved slices of reciprocal space can be recorded, and a volume of reciprocal space can be reconstructed from these consecutive slices.

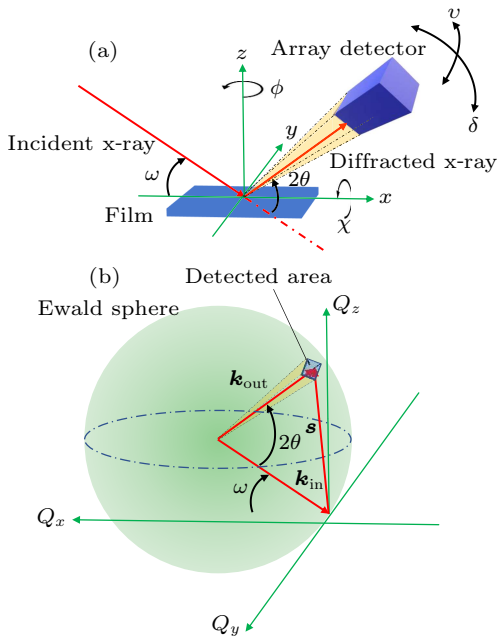


Fig. 1. Schematic diagram of 3D-RSM data collection. (a) Diffraction geometry of 3D-RSM conducted with a diffractometer and an array detector (ω, χ, and φ circles are three rotational degrees of freedom of the sample. Δ and υ circles are two rotational degrees of freedom of the array detector). The array detector spans a solid angle in the real space. (b) Schematic diffraction geometry of 3D-RSM in reciprocal space. The solid angle in real space represents a curved slice on the Ewald sphere in reciprocal space.

2.3. DC resistance–temperature measurement

DC resistance–temperature (R–T) dependence was measured in a physical property measurement system (PPMS) with four-terminal method. Resistance in both cooling and heating circles were recorded in order to minimize the deviation caused by thermoelectric effect. Superconducting critical temperature (T_C) was determined from the resistance jump.

2.4. Microwave surface resistance measurement

Microwave surface resistance of the films at 9.375 GHz was measured with the resonant cavity perturbation method. This technique has the required sensitivity for the measurement of R_S near T_C of HTSC.

The experiment apparatus is shown in Fig. 2. All measurements were carried out under the TE_{011} mode of the cavity, which causes no electrical field at lateral surface of the cavity. The resonant frequency ω_0 and band width $\Delta\omega$ can be obtained from the frequency response recorded by a vector network analyzer (Agilent N5230C): peak frequency is ω_0, the full width at half maximum (3-dB band width) is $\Delta\omega$. Then, the quality factor Q can be calculated from formula

$$Q = \omega_0/\Delta\omega, \tag{1}$$

In our experiment, the oxygen-free Cu cavity without sample insertion was first cooled down to 78 K by liquid nitrogen (Indium seals were used to ensure vacuum tight). Using formula (1), we obtain the unloaded resonant frequency $\omega_0 = 9.375$ GHz and quality factor $Q_0 = 112000$. Next, the sample was mounted on a sapphire rod and the sample-rod assembly was inserted into the cylindrical cavity through the hole drilled at the center of the bottom. Then, the loaded quality factor Q_S can also be obtained. The R_S of the film was eventually calculated from the Q difference using formula[25]

$$R_S = \left(Q_S^{-1} - Q_0^{-1}\right)/A_S, \tag{2}$$

where $A_S = 0.00036\ \Omega^{-1}$ is a calibration factor associated with cavity mode and geometry.

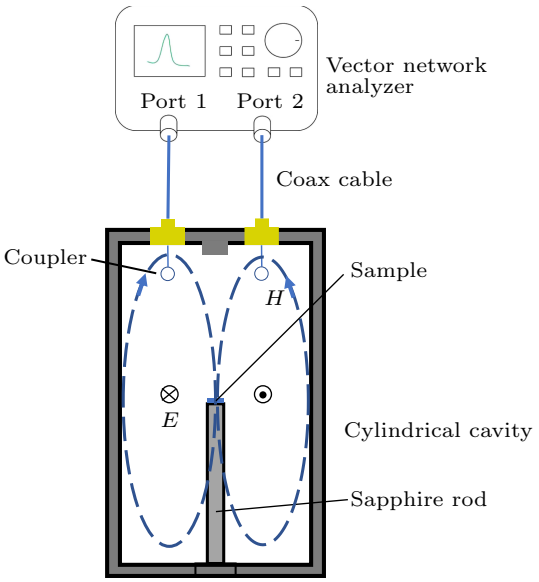


Fig. 2. The schematic diagram for the experimental apparatus of the resonant cavity perturbation method. The quality factors were all obtained under 78 K.

3. Results and discussion

3.1. Electrical properties

From the DC R–T dependence shown in Fig. 3(a), superconducting critical temperatures of the films are all around 90 K, indicating that they have approximately the same oxygen content, which coincides with former report.[20,26]

For 9.375-GHz microwave, the dependence of R_S at 78 K on oxygen pressure during deposition were plotted in Fig. 3(b). It shows that film grown under higher oxygen pressure has lower R_S. It is noticeable that sample #1 and sample #3 with similar DC electrical properties have more than an order of magnitude difference in microwave surface resistance.

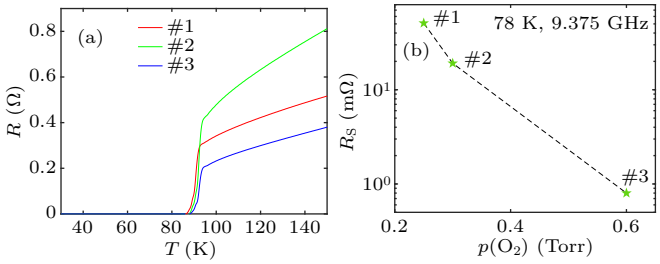


Fig. 3. (a) DC R–T dependence obtained with four-terminal method. The curve is the average of measurement results in cooling and heating circles. All curves show negligible differences in superconducting transition temperature. (b) Microwave surface resistance R_S of YBCO films at 78 K for 9.375-GHz microwave. It decreases with the increase of oxygen pressure deposition.

3.2. Microstructure characterization

The 3D-RSMs around YBCO (00l) (i.e., (004), (006), and (007)) diffraction peaks of samples #1, #2, and #3 are plotted in Figs. 4(a)–4(c), respectively. Although there are off-axis (e.g. (103) and (116)) spots shown up in the figures, their intensity is very weak and their corresponding grain content ($\sim 0.1\%$) is neglectable. So, only grains with c-axis, a-axis or b-axis normal to the surface of MgO (001) substrate exist in the films. We refer such oriented grains as c-grain, a-grain, and b-grain in the following discussion.

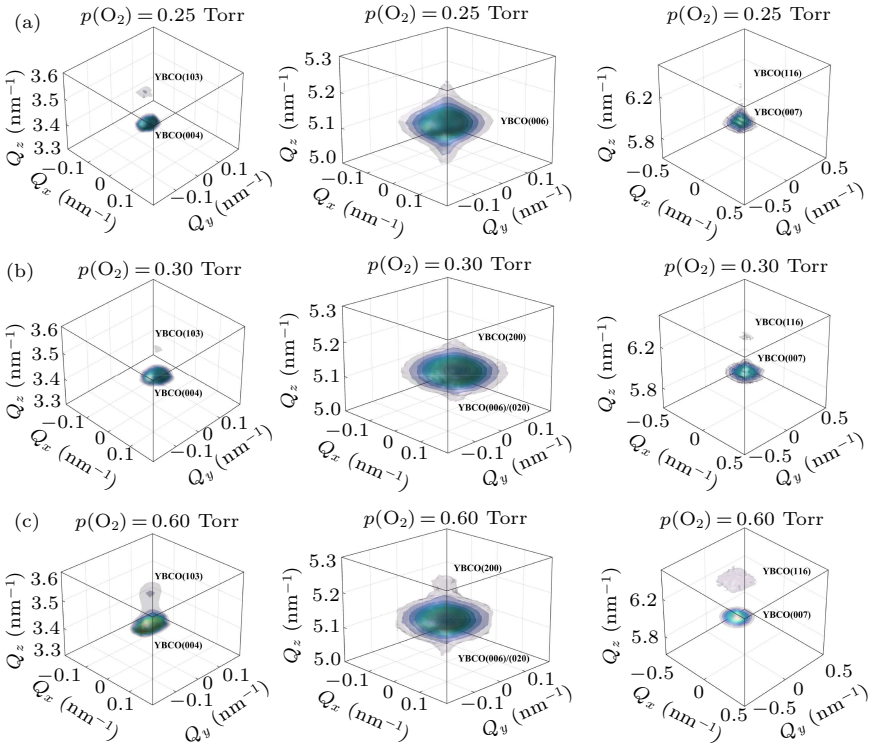


Fig. 4. The 3D-RSMs around YBCO (002), (006), and (007) diffraction peaks of (a) sample #1, (b) sample #2, and (c) sample #3. There exists YBCO (200) signal for sample #2 and sample #3. However, the intensity is very weak as compared with YBCO (006)/(020), indicating that a-grain content is neglectable.

From the figure, we found that there is no YBCO(200) signal for sample #1 and its signal shows up for sample #2. Then, the intensity further increases for sample #3. This means high oxygen pressure prompts *a*-grain formation. As the lattice parameter *b* is very close to *c*/3, it is hard to resolve them from (00*l*) diffractions. In our previous work, relative intensity of *b*-grain (108) and *c*-grain (109) was chosen to determine the contents of *b*-grain and *c*-grain.[27] However, (108)/(018) diffractions can also be used to determine content of *a*, *b*-grains. Shown in Figs. 5(a)–5(c) are the cross sections of *a*, *b*-grains (108)/(018) diffraction 3D-RSMs at $Q_z = 2.56$ nm^{-1}((108)/(018) diffraction of *c*-grain locates at different Q_z). It is found that there is no (108)/(018) signal for sample #1, while two weak peaks show up for sample #2, and the peaks get stronger for sample #3. They illustrate that neither *a*-grains nor *b*-grains exist in sample #1, and the *a*, *b*-grain content increases with the rise of oxygen pressure. However, the diffraction intensities of *a*, *b*-grains are much weaker than that of *c*-grains.

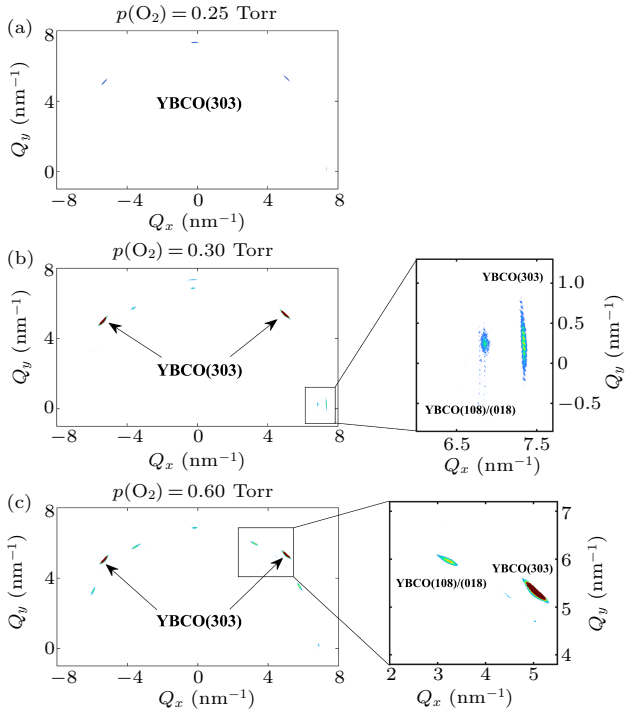


Fig. 5. The Q_x–Q_y cross sections at $Q_z = 2.56$ nm^{-1} for (a) sample #1, (b) sample #2, and (c) sample #3, which crosscut the 3D-RSMs of YBCO *a*, *b*-grain (108)/(018) diffraction. A portion of *c*-grain (303) diffraction signal is also recorded by the detector. The insets in panels (b) and (c) are the magnified view of selected zone in corresponding cross sections.

In order to get the relative content of *a*, *b* and *c*-grains, the 3D-RSMs of *c*-grain (108)/(018) for samples #1, #2, and #3 are also depicted in Figs. 6(a)–6(c). Listed in Table 1 are the integrated intensities $I(108/018)_{ab}$ of *a*, *b*-grains and $I(108/018)_c$ of *c*-grains for samples #1, #2, and #3. In all three samples, the content ratio γ between *a*, *b* grains and *c*-grains ($I(108/018)_{ab}/I(108/018)_c$) is less than 0.01. Therefore, the content of *a*, *b*-grains is neglectable, so all films are out-of-plane highly *c*-axis oriented. The result can be explained from different surface energy between (001) and (100)/(010) surface in YBCO. The low energy surfaces in YBCO are the ones perpendicular to the principal axis. Since YBCO (001) surface has a lower surface energy than YBCO (100)/(010), *c*-grains are more preferable. Moreover, the rise of $I(108/018)_{ab}$ further confirms that higher oxygen pressure during deposition contributes to *a*, *b*-grains growth. Former researches have revealed that *a*, *b*-grains follow island growth mode, while *c*-grains grow layer-by-layer.[28,29] Thus, the *c*-grains need higher oversaturation, so that the deposited particles can migrate a longer distance on the surface to step edges. When the oxygen partial pressure gets higher, collision between sputtered particles and supplied oxygen species becomes severe, and kinetic energy of deposited particles decreases. In that case, a few particles do not have sufficient kinetic energy to assist the migration. Therefore, they start to form *a*, *b*-grains, although *a*, *b*-grains are relatively unstable.

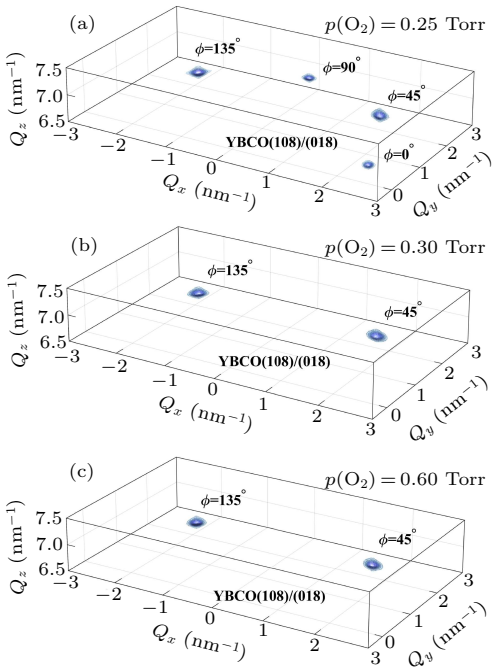


Fig. 6. The 3D-RSMs of *c*-grain (108)/(018) of (a) sample #1, (b) sample #2, and (c) sample #3. There exist 0° *c*-grains in sample #1, while samples #2 and #3 only contain 45° *c*-grains.

Table 1. The integrated intensity of diffraction spots (108)/(018) of *a*, *b*-grains ($I(108/018)_{ab}$) and *c*-grains ($I(108/018)_c$) for samples #1, #2, and #3. The content ratio γ between *a*, *b*-grains and *c*-grains is listed in the last row.

	$I(108/018)_{ab}$	$I(108/018)_c$	γ
#1	0	2.6×10^6	0
#2	1.8×10^3	2.6×10^6	0.001
#3	5.8×10^3	3.7×10^6	0.002

The Q_x–Q_y cross sections, which crosscuts the 3D-RSMs of *c*-grain (205)/(025) diffraction, are illustrated in Figs. 7(a)–7(c). According to the position of (205)/(025) diffraction, we calculated YBCO lattice parameter in each film. As shown in Table 2, the parameter is very close to the lattice constant of YBCO single crystal, and varies a little with the increase

of oxygen pressure. It implies that there is nearly no strain in the film. Moreover, the 3D-RSMs show that there are two in-plane orientations for *c*-grains: YBCO [100] ∥ MgO [100] and YBCO [100] ∥ MgO [110]. Therefore, we can assume that *c*-grains are 0° or 45° in-plane oriented. We denote the former 0° *c*-grains and the latter 45° *c*-grains. Again, their integrated intensity is listed in Table 3, while the 0° and 45° *c*-grain ratio are also listed at the last two rows. We found that there is about 22% 0° *c*-grains in the film deposited under low oxygen pressure (0.25 Torr), while those films deposited under high oxygen pressure (0.3 Torr and 0.60 Torr) contain only 45° *c*-grains.

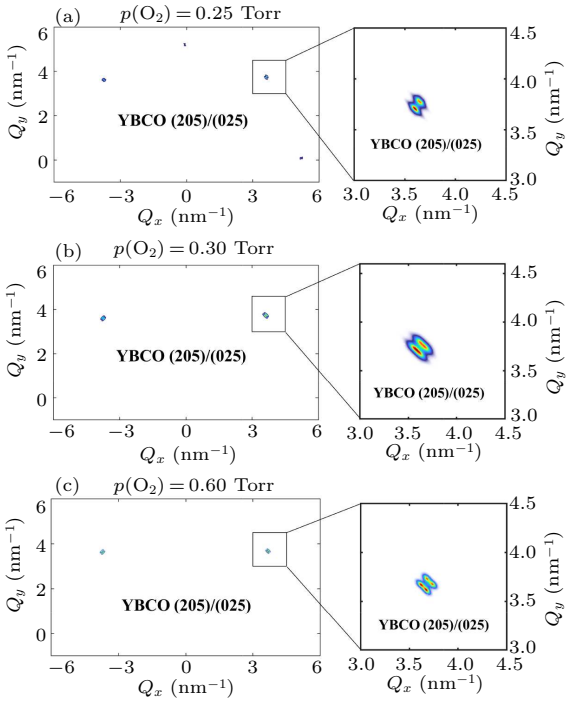


Fig. 7. The Q_x–Q_y cross sections of *c*-grain (205)/(025) 3D-RSMs (a) at $Q_z = 4.26$ nm^{-1} for sample #1, (b) at $Q_z = 4.27$ nm^{-1} for sample #2, and (c) at $Q_z = 4.28$ nm^{-1} for sample #3. The insets are the magnified view of the selected zone. It shows the difference between lattice parameter *a* and *b*, so it can be used for lattice parameter calculation.

Table 2. The lattice parameter of YBCO calculated from (205)/(025) diffraction of *c*-grain. It is very close to the lattice constant of YBCO single crystal.

	Sample #1	Sample #2	Sample #3	YBCO single crystal
a (nm)	0.381	0.382	0.382	0.382
b (nm)	0.387	0.387	0.388	0.389
c (nm)	1.174	1.170	1.169	1.168

Table 3. The content ratio of *c*-grains with 0° and 45° in-plane orientations (γ (0°) and γ (45°)). They were calculated from integrated (108)/(018) diffraction intensity ratio of corresponding *c*-grain.

c-grain content ratio	Sample #1	Sample #2	Sample #3
γ (0°)	22%	0%	0%
γ (45°)	78%	100%	100%

This phenomenon can be attributed to interface atomic configuration formed under different oxygen pressures. The formation probability of different in-plane orientations of grains depends on their terminal planes, which has a close relationship with the interface energy. In general, a more stable interface should be a lower energy cut. From transmission electron microscopy, 0° in-plane oriented grains terminate between Ba–O layer and Cu–O plane layer. In this mode, one YBCO unit lies above one MgO unit. For 45° in-plane oriented grains, the cut lies between Cu–O chain layer and Ba–O layer. In this mode, three YBCO units lies on two MgO units. The calculation result demonstrates that the minimum energy cut of YBCO lies between Cu–O chain layer and Ba–O layer. Therefore, 45° in-plane orientation is more favorable for YBCO *c*-grains. However, former study has revealed that 0° in-plane oriented grains form a more stable interfacial structure than 45° in-plane oriented grains in terms of the geometrical lattice matching. Meanwhile, in oxygen deficient state, the cut between Ba–O layer and Cu–O plane layer brings smaller dipole moment, thus the bond energy can be lower. This allows the growth of 0° in-plane oriented *c*-grains under relatively low oxygen pressure.[30–32]

Figure 8 plots the dependence of R_S on the diffraction intensity of 45° *c*-grains. Sample #1 has the lowest 45° *c*-grain diffraction intensity due to the coexistence of 0° and 45° *c*-grains, while samples #2 and #3 are composed only with 45° *c*-grains. Therefore, sample #1 inevitably has 45° in-plane tilt boundaries as compared with samples #2 and #3. Because the superconducting coherence length of YBCO is comparable with the grain boundary width, the superconducting coupling would be poor across the grain boundaries.[33,34] It has been found that the *I*–*V* characteristics of tilt boundaries across [001] grains are consistent with a superconductor–normal–superconductor-type weak-link behavior in $YBa_2Cu_3O_7$ films.[35] Therefore, 45° in-plane tilt boundaries would have a dominant effect on the increase of R_S.[36,37] As a result, sample #1 is expected a bigger R_S, qualitatively agreeing with the tendency of microstructure evolution.

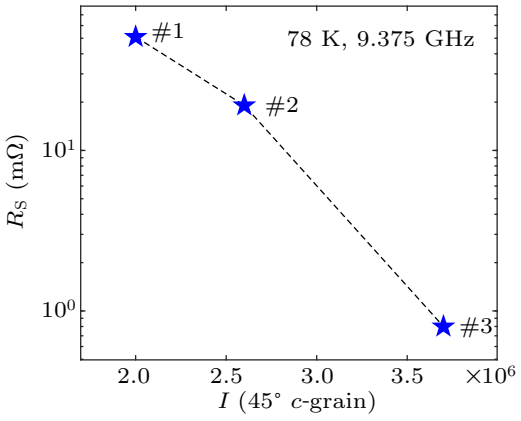


Fig. 8. Dependence of microwave surface resistance (R_S) on the diffraction intensity of 45° *c*-grain diffraction intensity. It shows that R_S decreases with the increase of 45° *c*-grain diffraction intensity.

However, there is about 20-mΩ difference in R_S for sam-

ples #2 and #3, with nearly no in-plane tilt boundaries and approximately same grain size. We noticed that the integrated diffraction intensity of *c*-grain (108)/(018) increases with the rise of oxygen pressure. Former studies have pointed out that the kinetic energy of deposited particles decrease as the oxygen pressure increases, so the deposition parameter would be farther away from the instability line for YBCO lattice formation. This would result in a more stable YBCO cells, with less position exchange between Y and Ba cations. Therefore, the diffraction intensity can be significantly increased, and brings nearly no change to the critical temperature for *in-situ* films. Furthermore, the YBCO cell with less cation disorder would have a smaller lattice parameter *c* because of stronger screening effect on Ba ions, which coincides with our experimental results.[38–42] Therefore, we deduced that a finer crystal structure with less cation disorder forms under relatively higher oxygen pressure. In that case, the higher R_S in sample #2 can be explained by more cation disorder in YBCO cells. This kind of defects would also cause the increase of R_S due to film lattice deformation.[43]

Despite of this, the oxygen pressure cannot be excessively high as the vacuum in the chamber would be destroyed, and the particle cannot vest the film with sufficient energy to form the perovskite structure.

4. Conclusion and perspectives

YBCO HTSC films were deposited on single crystal MgO (001) substrate under different oxygen pressures with PLD method and their microwave surface resistance was measured. It is found that the R_S drops significantly with the rise of the deposition oxygen pressure, while T_C varies little. To analyze the R_S dependence on the deposition oxygen pressure, the microstructure of these films was characterized by using synchrotron radiation 3D-RSM. We found that all the films are highly oriented with *c*-axis perpendicular to the surface. The relative content of *a*, *b*-grains increases with the oxygen pressure, due to the decrease of oversaturation. The *c*-grains are mainly 0° and 45° in-plane orientated. Under a higher oxygen pressure, *c*-grains tend to choose the latter mode because of the lower interface energy. Thus, the in-plane tilt grain boundaries between grain domains with different in-plane orientations vanish. Furthermore, we deduced that the cation disorder in YBCO lattice can also be decreased by raising the oxygen pressure to a certain extent during deposition, since the deposition parameters become farther away from the instability line in this process. With less tilt boundaries and crystal defects, the microwave surface resistance of the film would drop significantly.

Acknowledgements

Project support by the National Key Research and Development Program of China (Grant No. 2022YFA1603900), the National Natural Science Foundation of China – Beijing Joint Fund (Grant No. U23A6015), Central University Basic Research Fund of China (Grant No. E1E40207X2), and the Funds from University of Chinese Academy of Sciences (Grant Nos. E1EG0210X2 and 118900M018). The authors gratefully acknowledge beamtimes from 1W1A Diffuse x-ray Scattering Station in Beijing Synchrotron Radiation Facility and BL02U2 Surface Diffraction Station in Shanghai Synchrotron Radiation Facility.

References

[1] Sun L and He Y 2014 *IEEE Trans. Appl. Superd.* **24** 1
[2] Simon R W, Hammond R B, Berkowitz S J and Willemsen B A 2004 *Proc. IEEE* **92** 1585
[3] Magnuson M, Schmitt T, Strocov V N, Schlappa J, Kalabukhov A S and Duda L C 2014 *Sci. Rep.* **4** 7017
[4] Beasley M R 1989 *Proc. IEEE* **77** 1155
[5] Oh B, Char K, Kent A D, Naito M, Beasley M R, Geballe T H, Hammond R H, Kapitulnik A and Graybeal J M 1988 *Phys. Rev. B* **37** 7861
[6] Petrenko E V, Omelchenko L V, Terekhov A V, Kolesnichenko Yu A, Rogacki K, Sergeyev D M and Solovjov A L 2022 *Low Temp. Phys.* **48** 755
[7] Stangl A, Palau A, Deutscher G, Obradors X and Puig T 2021 *Sci. Rep.* **11** 8176
[8] Liu H, Xu Y, Liu F, Wang Y and Song Y 2019 *IEEE Trans. Microwave Theory Tech.* **67** 2720
[9] Long Z, Tian M, Zhang T, Qiao M, Wu T and Lan Y 2020 *IEEE Trans. Appl. Supercond.* **30** 1
[10] Zhao Y, Zhu J M, Jiang G Y, Chen C S, Wu W, Zhang Z W, Chen S K, Hong Y M, Hong Z Y, Jin Z J and Yamada Y 2019 *Supercond. Sci. Technol.* **32** 044004
[11] Jing D, Shao K, Cao C H, Zhang L X, Jiao G, Zhang Z J, Li S Q, Guo C N, Yang B C, Wang X P, Xiong G C and Lian Q J 1994 *Supercond. Sci. Technol.* **7** 792
[12] Turner C J, Stevenson T, Cantor R, Hilliard L, Murphy T E and Bulcha B 2023 *IEEE Trans. Appl. Supercond.* **33** 1
[13] Kalenyuk A A, Kasatkin A L, Futimsky S I, Pokusinskiy A O, Prikhna T A, Shapovalov A P, Shaternik V E and Akhmadaliev Sh 2023 *Supercond. Sci. Technol.* **36** 035009
[14] Chen T Y, Xia Y D, Zhao R P, Wu D, Feng Z P, Yang J T, Xin J J, Wang W, Jin K and Tao B W 2022 *Ceram. Int.* **48** 17837
[15] Rizzo F, Piperno L, Augieri A, Meledin A, Feighan J, MacManus-Driscoll J L and Celentano G 2025 *Physica C* **630** 1354648
[16] Bektas M, Birlik I and Celik E 2025 *Physica C* **629** 1354633
[17] Usoskin A, Betz U, Gnilsen J, Noll-Baumann S and Schlenga K 2019 *Supercond. Sci. Technol.* **32** 094005
[18] Celentano G, Rizzo F, Augieri A, Mancini A, Pinto V, Rufoloni A, Vannozzi A, MacManus-Driscoll J L, Feighan J, Kursumovic A, Meledin A, Mayer J and Van Tendeloo G 2020 *Supercond. Sci. Technol.* **33** 044010
[19] Vaimala T, Aye M M, Rivasto E, Zhao Y, Huhtinen H and Paturi P 2024 *Physica C* **624** 1354565
[20] Xiong P Y, Chen F C, Feng Z P, Yang J T, Xia Y D, Yuan Y F, Wang X, Yuan J, Wu Y, Shi J and Jin K 2023 *Chin. Phys. B* **32** 077402
[21] Zhou X H, Chen J, Liu Z Y and Cai C B 2024 *Ceram. Int.* **50** 6517
[22] Gaudet S, De Keyser K, Lambert-Milot S, Jordan-Sweet J, Detavernier C, Lavoie C and Desjardins P 2013 *J. Vac. Sci. Technol. A* **31** 021505
[23] Thanh T N, Blanc N, Boudet N, Bourjot E, Zhiou S, Kovacova V, Rodriguez P, Nemouchi F and Gergaud P 2015 *IEEE International Interconnect Technology Conference and* 2015 *IEEE Materials for Advanced Metallization Conference (IITC/MAM)*, May 18–21, 2015, Grenoble, France, p. 53

[24] Gorfman S, Spirito D, Zhang G, Detlefs C and Zhang N 2022 *Acta Cryst A* **78** 158
[25] Sridhar S and Kennedy W L 1988 *Rev. Sci. Instrum.* **59** 531
[26] Jorgensen J D, Veal B W, Paulikas A P, Nowicki L J, Crabtree G W, Claus H and Kwok W K 1990 *Phys. Rev. B* **41** 1863
[27] Yi Q R, Xiong P Y, Wang H H, Li G, Wang Y K, Dong E Y, Chen Y, Shen Z B, Wu Y, Yuan J, Jin K and Gao C 2023 *Acta Phys. Sin.* **72** 046101 (in Chinese)
[28] Terashima T, Bando Y, Iijima K, Yamamoto K, Hirata K, Hayashi K, Kamigaki K and Terauchi H 1990 *Phys. Rev. Lett.* **65** 2684
[29] Wen C T and Tseung Y T 1997 *Jpn. J. Appl. Phys.* **36** 76
[30] Matsuda J S, Oba F, Murata T, Yamamoto T, Ikuhara Y, Mizuno M, Nomura K, Izumi T and Shiohara Y 2004 *J. Mater. Res.* **19** 2674
[31] Wang X, Cai Y Q, Yao X, Wan W, Li F H, Xiong J and Tao B W 2008 *J. Phys. D: Appl. Phys.* **41** 165405
[32] Miletto G F and Scotti U U 1997 *J. Alloys Compd.* **251** 56
[33] Camps R A, Evetts J E, Glowacki B A, Newcomb S B, Somekh R E and Stobbs W M 1987 *Nature* **329** 229
[34] Dimos D, Chaudhari P, Mannhart J and LeGoues F K 1988 *Phys. Rev. Lett.* **61** 219
[35] Mannhart J, Chaudhari P, Dimos D, Tsuei C C and McGuire T R 1988 *Phys. Rev. Lett.* **61** 2476
[36] Kusunoki M, Takano Y, Mukaida M and Ohshima S 1999 *Physica C* **321** 81
[37] Young K H and Sun J Z 1991 *J. Appl. Phys.* **70** 3748
[38] Endo T, Yoshii K, Iwasaki S, Kohmoto H, Saratani H, Shiomi S, Matsui M and Kurosaki Y 2003 *Supercond. Sci. Technol.* **16** 110
[39] Eom C B, Sun J Z, Yamamoto K, Marshall A F, Luther K E, Geballe T H and Laderman S S 1989 *Appl. Phys. Lett.* **55** 595
[40] MacManus-Driscoll J L, Alonso J A, Wang P C, Geballe T H and Braviman J C 1994 *Physica C* **232** 288
[41] Matijasevic V, Rosenthal P, Shinohara K, Marshall A F, Hammond R H and Beasley M R 1991 *J. Mater. Res.* **6** 682
[42] Shapovalov A P, Boguslavskij Y M, Ruban A I, Gridneva G G, Melnikov V S and Pshentsova N P 1992 *Supercond. Sci. Technol.* **5** 283
[43] Vorobiev A K, Drozdov Y N, Gusev S A, Mironov V L, Vostokov N V, Kluenkov E B, Gaponov S V and Talanov V V 1999 *Supercond. Sci. Technol.* **12** 908